ACS APPLIED MATERIALS & INTERFACES

Open Access
This article is licensed under CC-BY 4.0

www.acsami.org
Forum Article

Switchable 3D Photonic Crystals Based on the Insulator-to-Metal Transition in VO_2

Published as part of ACS Applied Materials & Interfaces special issue "Porous Semiconductor Science and Technology Conference - PSST 2024".

Jun Peng, Julia Brandt, Maurice Pfeiffer, Laura G. Maragno, Tobias Krekeler, Nithin T. James, Julius Henf, Christian Heyn, Martin Ritter, Manfred Eich, Alexander Yu. Petrov, Kaline P. Furlan, Robert H. Blick, and Robert Zierold*

Cite This: *ACS Appl. Mater. Interfaces* 2024, 16, 67106−67115

Read Online

ACCESS | Metrics & More | Article Recommendations | Supporting Information

ABSTRACT: Photonic crystals (PhCs) are optical structures characterized by the spatial modulation of the dielectric function, which results in the formation of a photonic band gap (PBG) in the frequency spectrum. This PBG blocks the propagation of light, enabling filtering, confinement, and manipulation of light. Most of the research in this field has concentrated on static PhCs, which have fixed structural and material parameters, leading to a constant PBG. However, the growing demand for adaptive photonic devices has led to an increased interest in switchable PhCs, where the PBG can be reversibly activated or shifted. Vanadium dioxide (VO_2) is particularly notable for its near-room-temperature insulator-to-metal transition (IMT), which is accompanied by significant changes in its optical properties. Here, we demonstrate a fabrication strategy for switchable three-dimensional (3D) PhCs, involving sacrificial templates and a VO_2 atomic layer deposition (ALD) process in combination with an accurately controlled annealing procedure. The resulting VO_2 inverse opal (IO) PhC achieves substantial control over PBG in the near-infrared (NIR) region. Specifically, the synthesized VO_2 IO PhC exhibits PBGs near 1.49 and 1.03 μm in the dielectric and metallic states of the VO_2 material, respectively, which can be reversibly switched by adjusting the external temperature. Furthermore, a temperature-dependent switch from a narrow-band NIR reflector to a broad-band absorber is revealed. This work highlights the potential of integrating VO_2 into 3D templates in the development of switchable photonics with complex 3D structures, offering a promising avenue for the advancement of photonic devices with adaptable functionalities.

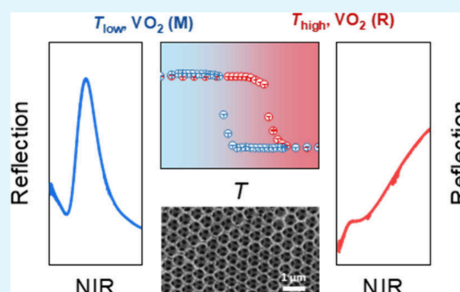

KEYWORDS: *switchable photonics, vanadium dioxide, insulator-to-metal transition, atomic layer deposition, inverse opal*

Downloaded via TU HAMBURG-HARBURG on January 2, 2025 at 17:21:19 (UTC).
See https://pubs.acs.org/sharingguidelines for options on how to legitimately share published articles.

■ INTRODUCTION

Photonics, the science and technology of generating, controlling, and detecting photons, have emerged as a cornerstone in modern engineering and scientific research. The manipulation of light has led to transformative advancements across various fields including telecommunications, sensing, imaging, and computing. Central to many of these advancements are PhCs—periodic nanostructures that possess unique optical properties due to their ability to control light propagation through PBGs and resonant modes,[1,2] which are essential to various cutting-edge applications including metasurfaces, photonic integrated circuits, and photonic diagnosis.[3−5] However, conventional static PhCs are limited by their lack of *in operando* tunability. This limitation restricts their adaptability and versatility, particularly in dynamic environments where the optical properties need to be adjusted in real-time in response to external stimuli.[6,7] To address this challenge, researchers have focused on developing adjustable photonics, where the optical properties, such as the photonic band structure, resonance frequencies, and light propagation can be dynamically altered,[8,9] enabling new possibilities for designing adaptive optical devices with enhanced functionality and performance.

VO_2 stands out as a promising material for switchable photonics because of its near-room-temperature IMT, which is accompanied by significant changes in optical and electronic properties.[10−16] In recent years, many studies have explored the use of VO_2 to construct periodic structures or to integrate VO_2 with such structures for various applications.[17−20] For example, sol−gel infiltrated VO_2 integrated into core/shell 2D

Received: August 15, 2024
Revised: November 1, 2024
Accepted: November 19, 2024
Published: December 2, 2024

ACS Publications
© 2024 The Authors. Published by American Chemical Society

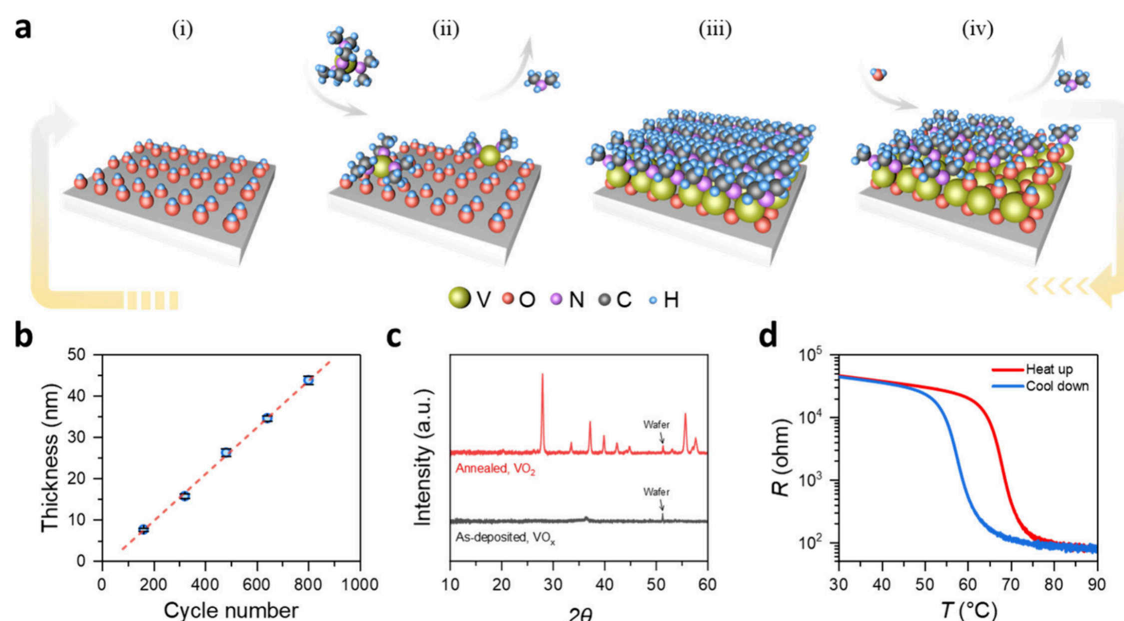

Figure 1. ALD deposition of VO_2 thin film. (a) Mechanism of VO_x film deposition via ALD. This diagram illustrates the ligand-exchange process during the ALD cycles, showing how the surface becomes terminated with (i) −OH groups and (iii) $-NMe_2$ groups after (iv) the H_2O and (ii) the TDMAV pulses, respectively. (b) Thickness of the deposited films as a function of the number of ALD cycles, demonstrating a constant GPC of 0.56 Å/cycle. (c) GIXRD spectra for the as-deposited VO_x film and annealed VO_2 film. In the annealed VO_2 film, the peak near $2\theta = 51°$ belongs to the substrate, while other peaks belong to VO_2. A more detailed labeling is shown in Figure S1. (d) Temperature-dependent resistance measurement of the annealed VO_2 film, revealing the IMT with over 3 orders of magnitude change in resistance.

PhC has been used to adjust the color for thermochromic smart window applications.[21] Hybrids of crossed gold nanoantenna arrays and VO_2 thin films synthesized by chemical vapor deposition have achieved reversible switching for nanoscale optical memory functionalities.[22] Alternatively, sputtered VO_2 thin films integrated with metal metasurfaces have been utilized as optical switches, optical limiters with adjustable thresholds, and nonlinear optical isolators.[23] Despite these advancements, most VO_2 integrations have been limited to 1D or 2D structures, with few attempts at 3D structures due to material synthesis challenges.[24−26]

As an advanced surface-limited coating technique, ALD offers precise conformality on 3D complex structures. Previous studies have demonstrated the deposition of VO_2 thin films on a variety of planar substrates,[27−33] indicating the potential for integrating VO_2 into 3D photonic structures such as 3D PhCs. By exploiting the change in the optical parameters induced by the VO_2's IMT, the optical properties of integrated photonics can be dynamically modulated. In this work, we first demonstrate VO_2 thin film synthesis via a combination of ALD and postdeposition annealing. The temperature-dependent IMT in the annealed thin film, transitioning from a low-temperature dielectric monoclinic phase VO_2 (M) to a high-temperature rutile metallic phase VO_2 (R), is investigated from electrical, structural, and optical perspectives. Subsequently, we successfully fabricated a VO_2 IO PhC using a process adapted from the VO_2 thin film deposition process to a polystyrene (PS) opal template. The fabricated VO_2 IO PhC demonstrates PBGs at approximately 1.49 and 1.03 μm in the dielectric and metallic states of the VO_2 material, respectively. Significantly, these PBGs can be reversibly switched by altering the external temperature. Additionally, a switch from a narrow-band NIR reflector to a broad-band absorber is observed in the dielectric and metallic state, respectively. The successful realization of VO_2 IO PhC demonstrates the feasibility of integrating ALD-based VO_2 with complex 3D structures, which opens up new opportunities for switchable photonics in adaptive and versatile optical devices.

RESULTS AND DISCUSSION

VO_2 Thin Film via ALD. The screening of suitable ALD precursors to later produce the 3D IO PhCs should meet two key conditions: (1) the precursor should not undergo chemical reactions with PS that would alter the polymer structure or degrade the template, and (2) ALD deposition should occur below the stable temperature for ALD processing of PS, which is approximately 100 °C. Attracted by the interesting IMT property, the ALD community has already reported several precursors for the successful synthesis of VO_x films, including $VOCl_3$, VCl_4, $VO(OC_3H_7)_3$, tetrakis(ethylmethylamino)vanadium ($V(NEtMe)_4$, TEMAV), tetrakis(dimethylamino)vanadium ($V(NMe_2)_4$, TDMAV).[26,34,35] Among them, TEMAV has been the subject of most detailed studies.[27−30] However, in the reported literature, only the combination of TDMAV and H_2O has revealed a self-limited deposition of a dense VO_x film below 100 °C, which could then be converted into VO_2 via a postdeposition annealing process.[32,33,36] Therefore, we selected H_2O and TDMAV as precursors for oxygen and vanadium sources, respectively. According to the ligand-exchange mechanism which is commonly suggested for dimethylamino metal precursors, e.g., $Zr(NMe_2)_4$, $Zr(NEtMe)_4$, $Hf(NMe_2)_4$, $Hf(NEtMe)_4$,[37,38] the postulated deposition mechanism during the exposure ALD mode can be present in Figure 1a. During the first ALD half-cycle, the surface, saturated with hydroxyl groups (−OH) is exposed to and fully reacts with the TDMAV precursor, leaving $-NMe_2$ groups at the surface. The byproduct $HNMe_2$ and excessive TDMAV are pumped out in the following purging step. Then in the second half-cycle, the $-NMe_2$ groups connected to the V atom react with the second precursor, H_2O, forming a −OH group-terminated

https://doi.org/10.1021/acsami.4c13789
ACS Appl. Mater. Interfaces 2024, 16, 67106−67115

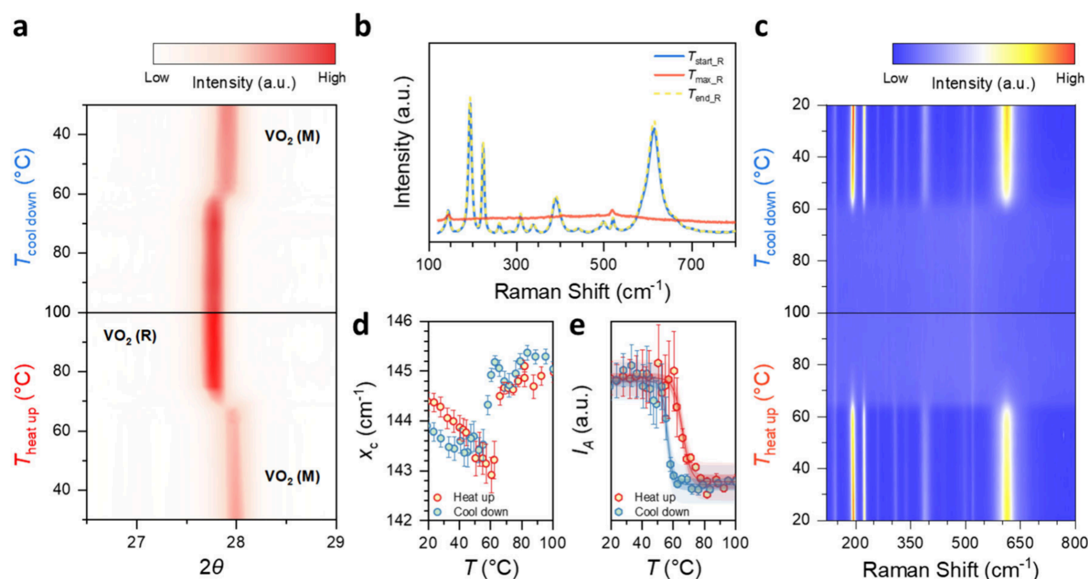

Figure 2. IMT characterization of VO_2 thin film. (a) *In situ* temperature-dependent GIXRD measurement zoomed in near $2\theta = 28°$ region. The peak shown belongs to the (011) plane of VO_2 (M) at low temperature while the (110) plane of VO_2 (R) at high temperature. (b) Raman spectra at low and high temperature. (c) Temperature-dependent Raman measurement. The peak at ∼520 cm^{-1}, which remains almost unaltered, is the signal from the SiO_2/Si substrate. Lorentz fitting analysis for (d) the peak position shift and (e) the peak area as peak intensity at ∼144.5 cm^{-1} as a function of temperature.

surface again after the H_2O pulse and purge step. As the deposition cycles continue, the thickness of VO_x increases linearly with the number of cycles.

The deposition temperature is set at 95 °C, where a constant deposition rate, usually termed growth per cycle (GPC), of 0.56 Å/cycle is obtained (Figure 1b). In agreement to earlier reports,[32,33,36] the as-deposited film is an amorphous VO_x film (Figure 1c and Figure S1a). After a postdeposition annealing process referring to the parameter's ranges used for thermal treatments of VO_x deposited by TEMAV (see Material and Methods),[27,29] the VO_x film is converted into a polycrystalline VO_2 film in the monoclinic $P2_1/c$ space group (Figure 1c and Figure S1b). The annealing treatment not only adjusts the stoichiometry and crystallinity but also causes changes in the film morphology, i.e., in roughness and thickness. Specifically, for a 33.6 nm thick as-deposited film, its roughness increases from 0.57 to 1.63 nm after annealing (Figure S2); and for a thicker as-deposited film of 140 nm thickness, a shrinkage of about 2% of the height is observed after the same annealing process (Figure S3). This slight change in morphology can be attributed to the more regular and orderly arrangement of atoms in polycrystalline VO_2 films compared with amorphous VO_x films after postdeposition annealing. The resistance change over temperature is one of the most important indicators of the VO_2 IMT performance. The temperature-dependent resistance measurement (Figure 1d) exhibits an IMT with over 3 orders of magnitude, accompanied by a hysteresis width of 10.3 °C (Figure S4), which is comparable to VO_2 synthesized by other synthetic methods, such as pulsed laser deposition[39] and molecular beam epitaxy.[40,41]

Structural Characterization of the VO_2 Thin Film. The negligible morphological change and impressive electrical IMT performance indicate the feasibility of ALD in constructing VO_2-based 3D structures. Furthermore, the quality of the ALD-based VO_2 thin films is verified by detailed grazing incidence X-ray diffraction (GIXRD) and Raman characterization during *in situ* heating and cooling processes. In the *in situ* temperature-dependent GIXRD measurement shown in Figure 2a, a small shift of approximately 0.15° is observed at around 68 and 60 °C during heating and cooling, respectively, for the most intense peak near $2\theta = 28°$ representing the (011) plane of VO_2 (M). The shifted peak at elevated temperatures represents the (110) plane of VO_2 (R), indicating the expected reversible transition from the VO_2 (M) phase to VO_2 (R) phase.[28,42,43] To ensure no other remanent phase changes occurred in the samples during the *in situ* experiments, the samples were also measured by GIXRD before and after the heating/cooling cycles covering a broader range of 2θ from 10° to 60°. The resulting diffractogram depicted in Figure S1b indicates a reversible IMT change without irreversible phase transformation within the film.

Additionally, Raman spectra of the annealed thin film at near room temperature, i.e., T_{start_R} = 19.4 °C and T_{end_R} = 19.1 °C in Figure 2b, exhibit distinct peaks at 144.5, 195.0, 224.8, 261.6, 285.7, 310.3, 338.9, 390.28, 440.2, 499.6, 613.8 cm^{-1}, corresponding to the VO_2 (M) phase, which agrees well with previous reports on crystalline VO_2.[41,44−47] The thin film's structural phase transition is monitored by temperature-dependent Raman spectroscopy (Figure 2c). Existing Raman peaks associated with the VO_2 (M) are expected to disappear above the transition temperature, i.e., when the film changes to the VO_2 (R) phase.[45] During the heating process, the intensity of all Raman peaks gradually decreases with increasing temperature. Above 65 °C up to the highest test temperature, T_{max_R} = 103.4 °C all peaks belonging to VO_2 disappear, except the peaks at about 144.5 and 520.0 cm^{-1}. The peak at 520.0 cm^{-1} belongs to the silicon substrate, and as expected, a linear redshift of this peak is observed as the temperature increases (Figure S5a). The peak at 144.5 cm^{-1} is associated with the VO_2 (M) and experiences a redshift below the transition temperature, while a significant blueshift is followed above the transition temperature, as displayed in Figure 2d. Noticeably, other VO_2 peaks also show a similar redshift as shown in Figure S5b, c before disappearance. During the subsequent

https://doi.org/10.1021/acsami.4c13789
ACS Appl. Mater. Interfaces 2024, 16, 67106−67115

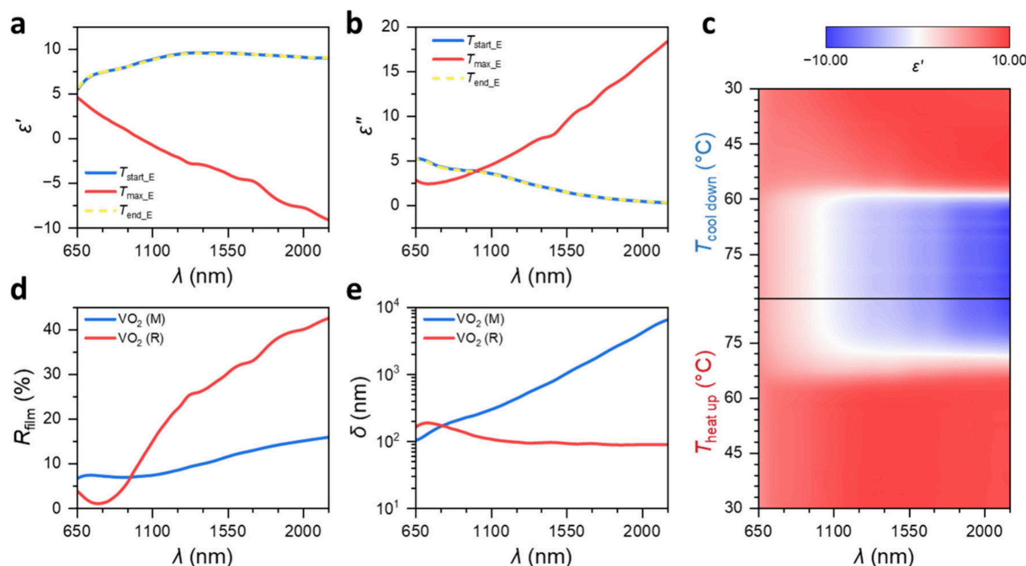

Figure 3. Optical characterization of ALD-deposited VO_2 thin film. (a) The real permittivity ε' and (b) the imaginary permittivity ε' at the start (T_{start_E}), maximum (T_{max_E}), and end (T_{end_E}) temperatures during a continuous heating/cooling measurement obtained from spectroscopic ellipsometry as a function of wavelength λ. Note that the lines for T_{start_E} and T_{end_E}, plotted as a solid blue line and a dashed yellow line in (a) and (b), overlap. This match indicates a fully reversible change in the optical properties of the film. (c) Colormap of ε' versus wavelength λ and temperature. (d) The film reflectance R_{film} converted from ε' and ε'', taking the temperature at T_{start_E} as VO_2 (M), and at T_{max_E} as VO_2 (R). (e) Skin depth δ for the VO_2 (M) and VO_2 (R) phases plotted logarithmically. The skin depth increases significantly toward long wavelengths in the VO_2 (M) phase while remaining constant in the VO_2 (R) phase.

cooling process, the peaks reappear at around ~60 °C, and gradually increase in intensity with decreasing temperature. A similar pattern has been reported for single crystal VO_2.[48,49] The temperature-dependent redshift can be explained by thermal lattice expansion, which results in a decrease in the phonon frequency. However, the arising blueshift at the transition temperature points to an increase in phonon frequency, which can be attributed to a lattice contraction.[46] Such a lattice contraction is associated with the phase transition between the VO_2 (M) and VO_2 (R) phases, which is consistent with the *in situ* GIXRD results. Upon heating, the 144.5 cm^{-1} peak's intensity defined over the peak area also experiences an obvious decrease due to the IMT (Figure 2e). This observed behavior of the ALD-deposited VO_2 films is consistent with previous reports on strain studies of an epitaxial VO_2 film[41] and single-crystal nanobeams.[49] Additionally, the overlapping curves from multiple temperature-dependent resistance tests on the same film sample, along with consistent Raman spectra before and after cyclic testing, indicate that the synthesized VO_2 exhibits excellent reversible switching durability in terms of both performance and structural integrity (Figure S6).

Optical Properties of the VO_2 Thin Film. To better understand the optical properties of the ALD-deposited VO_2, *in situ* temperature-dependent spectroscopic ellipsometry is used to characterize the change in complex permittivity $\tilde{\varepsilon}(\lambda) = \varepsilon' + i\varepsilon''$ of the thin film on the Si substrate over the wavelength λ during the IMT, where ε' and ε'' are the real part and the imaginary part of the complex permittivity $\tilde{\varepsilon}(\lambda)$, respectively. This measurement starts at room temperature T_{start_E} = 25.7 °C, heats to a temperature T_{max_E} = 88.4 °C, that is above the transition temperature, and then cools back to near room temperature T_{end_E} = 27.8 °C. Both ε' (Figure 3a) and ε'' (Figure 3b) reveal distinct differences between the low temperature (T_{start_E}, T_{end_E}) and the high temperature (T_{max_E}) states. Note, the typical value of ε' of a metal is negative, while that of a dielectric exceeds 1. At low temperatures, ε' of the VO_2 thin film indicates optically lossy dielectric behavior over the entire measured wavelength range. Whereas, at elevated temperatures, ε' remains above 1 only for wavelengths shorter than 1 μm, indicating that the VO_2 thin film, despite the change in value, retains lossy dielectric characteristics in this wavelength region. In contrast, for wavelengths longer than 1 μm, ε' becomes negative, revealing metallic optical characteristics. Limiting the discussion to this long wavelength range, these results demonstrate that the crystalline phase transition induces a pronounced change in optical properties. This observation is in good agreement with other reported VO_2 thin films produced by sputtering or sol–gel.[20,50−52] Specifically, the film begins its optical transition to the metallic VO_2 (R) phase at ~70 °C during heating and transitions back to the dielectric VO_2 (M) phase at ~60 °C during the following cooldown process, as shown in the temperature-dependent colormaps of ε' and ε'' in Figure 3c and Figure S7a, respectively. In addition, similar to the resistive and structural transitions, the optical transition also presents a hysteresis in the heating and cooling process. The film reflectance R_{film} can be mathematically obtained with the transfer-matrix method from the measured $\tilde{\varepsilon}(\lambda)$ (Figure S7b).[53] All the colormaps show a distinct IMT between the VO_2 (M) and VO_2 (R) phases during the heating and cooling processes. When R_{film} is plotted as line curves, the optical effect of the IMT on the reflection can be clearly seen (Figure 3d). The skin depth δ, which is the distance an electromagnetic wave travels through a material before its power is reduced to $1/e^2$, is used to explain the optical attenuation characteristics of VO_2. It can be calculated using the equation $\delta = \left(\frac{4\pi}{\lambda}k\right)^{-1}$ derived from the relation $\tilde{n}(\lambda) = \sqrt{\tilde{\varepsilon}(\lambda)}$, where $\tilde{n}(\lambda) = n + ik$ is the complex refractive index, and n and k are its real and imaginary part, respectively.[54] The skin depth of the low

https://doi.org/10.1021/acsami.4c13789
ACS Appl. Mater. Interfaces 2024, 16, 67106−67115

temperature VO_2 (M) phase increases towards longer λ values, as shown in Figure 3e. In contrast, the skin depth is relatively constant in the high temperature VO_2 (R) phase and remains below 200 nm over the entire λ range considered. Moreover, the detailed n and k also reveal a distinct difference between the VO_2 (M) and VO_2 (R) phases (Figure S8).

Fabrication of a VO_2 IO PhC. All of the above results, coupled with the inherent conformality and Angstrom-level controllability of ALD coatings, render the ALD-based VO_2 synthesis process a suitable candidate for fabricating switchable 3D photonic structures. By exploiting the pronounced reflectivity switching of VO_2 in the NIR region induced by temperature changes, alongside the presence of a PBG of the PhC structure, we devised a controllable PhC with an IO structure. This PhC allows for active control of the PBGs through temperature switching, combining a narrow-band NIR reflector—determined by the PhC's PBG, and a broad-band absorber given by the material's properties. The fabrication details are described in the Materials and Methods section. The successfully fabricated VO_2 IO PhC is shown in Figure 4.

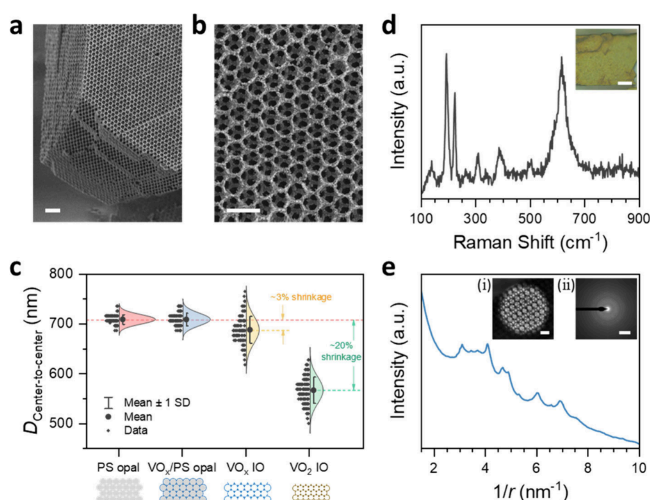

Figure 4. VO_2 IO PhC fabrication. SEM images of the VO_2 IO (a) from the side view at low magnification and (b) from the top view at higher magnification. (c) Statistics of center-to-center distance, $D_{Center-to-center}$, between adjacent PS spheres or macropores during the IO fabrication process: (I) Pristine PS opal template, (II) VO_x coated PS opal template (VO_x/PS opal), (III) VO_x IO, and (IV) VO_2 IO PhC. The $D_{Center-to-center}$ is measured using ImageJ software on the corresponding SEM images. The distribution curves were normalized according to the area under the curve. (d) Raman spectrum for the VO_2 IO. Inset: optical image of the VO_2 IO. (e) Radially averaged profiles of the IO lamella's electron diffraction ring using TEM before and after a heating/cooling cycle showing an unchanged VO_2 phase. Inset (i): TEM image for the VO_2 IO lamella. Inset (ii): corresponding electron diffraction pattern. Scale bars for (a), (b), (d-inset), (e-inset (i)), and (e-inset (ii)) are 2 μm, 1 μm, 20 μm, 500 nm, and 5 nm^{-1}, respectively.

The VO_2 IO exhibits a 3D periodic and ordered multilayer porous structure throughout, from top to bottom, as presented in Figure 4a. This homogeneity demonstrates that the ALD coating is conformal within the opal structure. Figure 4b further highlights the high uniformity and regularity of the pore arrangement. Additionally, the stability of the IO structure is conserved upon heat treatment and crystallization. However, compared to the pristine PS opal template, the VO_2 IO experiences significant shrinkage (Figure S9). The center-to-center distance, $D_{Center-to-center}$, between adjacent PS spheres or macropores at different stages in the fabrication process is statistically compared, as shown in Figure 4c. The $D_{Center-to-center}$ between adjacent PS spheres in the pristine template is 708.7 ± 9.66 nm. After VO_x ALD coating, the $D_{Center-to-center}$ between adjacent VO_x-coated PS spheres is 708.6 ± 12.67 nm, remaining almost unchanged. But after removal of the PS template performed at 390 °C in vacuum (Materials and Methods, Figure S10), the $D_{Center-to-center}$ between adjacent macropores decreases to 687.8 ± 27.05 nm, accounting for a shrinkage of approximately 3%. During the subsequent annealing process to adjust the IO shell composition from VO_x to VO_2, the $D_{Center-to-center}$ between adjacent macropores further shrinks significantly to 566.7 ± 24.45 nm, resulting in a further shrinkage of approximately 17.6%. Overall, compared to the pristine PS opal template, the VO_2 IO shrinks by approximately 20%. This observed shrinkage is about double the value previously observed for zirconia, titania, and mullite IOs.[55−57] However, in our work, we expect that not only crystallization would occur but also phase transitions between different vanadium oxide phases with an associated shrinkage of the unit cell. Thus, the hereby observed shrinkage has the contribution from the thermal shrinkage related to crystallization as observed in other reports,[55−57] as well as the material phase change. In addition to the 3D morphology change in macropore size, the material itself undergoes a complex process and is successfully converted into VO_2 by a final postdeposition annealing step. The Raman spectrum of such a prepared IO is highly consistent with that of the VO_2 film as shown in Figure 4d, which indicates that the skeleton of IO is indeed pure VO_2 with the V oxidation state +4. Thus, the additional shrinkage from the calcined VO_x IO to the VO_2 IO is attributed to the change in oxidation state and not to solely crystallization. However, to fully understand the volume shrinkage, it is necessary to determine the precise VO_x stoichiometry in all manufacturing stages. Additionally, a piece of an IO lamella (Figure S11) is prepared to further study the VO_2 IO structure by using transmission electron microscopy (TEM). The radial distribution profile of the IO lamella's electron diffraction ring matches well with the same PDF card used for thin film XRD matching (Figure 4e, Figure S12). This agreement also confirms the successful fabrication of an IO made out of VO_2. In addition, the composition and microstructure of the VO_2 IO lamella remains unchanged after being heated to 100 °C and then cooled back to room temperature (Figure S12).

Switchable Photonics Characterization. Detailed reflection spectra R_{IO} of the VO_2 IO PhC are recorded during *in situ* heating and cooling. At low temperatures, when the VO_2 is in the dielectric state (M), e.g., at T_{start_IO} = 30 °C, a distinct PBG is identified in the NIR region with the center position of the Bragg peak $\lambda_c \approx 1.49$ μm, as shown in temperature-dependent R_{IO} in Figure 5a. This PBG is induced by the IO structure consisting of face-centered cubic stacked sphere-shaped air cavities embedded in the VO_2 backbone, forming a periodic permittivity alteration. When the temperature rises above 80 °C, this peak in the NIR wavelength range vanishes due to the IMT from VO_2 (M) into VO_2 (R), which is the metallic phase, and a small peak at around $\lambda_c \approx 1.03$ μm is observed. The occurrence of this peak can be attributed to the transition in optical parameters due to the IMT, as estimated in Note 1. Note that this peak is not as pronounced as that observed in the dielectric VO_2 (M) phase since the real part of

https://doi.org/10.1021/acsami.4c13789
ACS Appl. Mater. Interfaces 2024, 16, 67106−67115

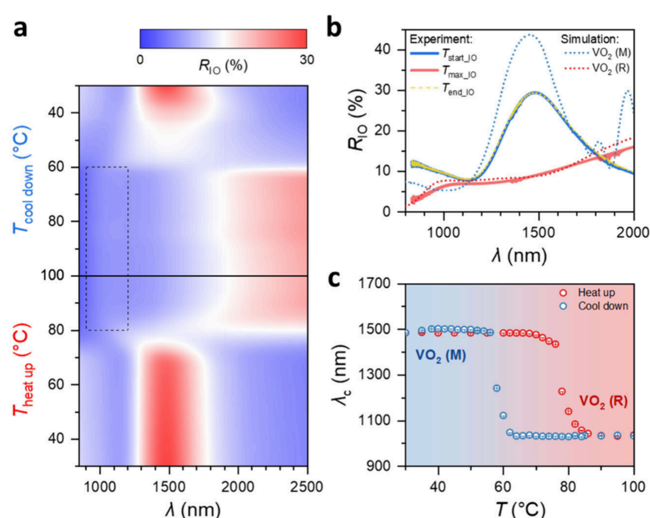

Figure 5. Switchable PBG of VO_2 IO PhC. (a) Reflection spectra R_{IO} during a heat-up and following cool-down measurement. (b) Experimental R_{IO} and simulated R_{IO} at high and low temperatures. The experimental results for T_{start_IO} and T_{end_IO} overlap. The small peak in the 900−1200 nm region of the curve marked as T_{max_IO} in (b) is highlighted in the roughly corresponding region with a black dashed box in (a). The oscillation in the simulated spectrum of the VO_2 (M) phase results from Fabry−Perot interference. (c) The Bragg peak position λ_c as a function of temperature, showing a switch function adapted to the external temperature. The Bragg peak position λ_c shifts from about 1.49 μm below the IMT transition temperature to about 1.03 μm above the IMT transition temperature.

the refractive index, n, of VO_2 in the VO_2 (R) phase is considerably lower than that in the VO_2 (M) phase, while the imaginary part, k, is higher (Figure S8). This fact implies that the reflection at each stacking layer is small. Hence, only a fraction of the incident light power is reflected, whereas the majority penetrates the structure and is absorbed. Moreover, due to increased absorption, the peak spectrally widens, making it less pronounced. In addition, similar to the R_{film} of the VO_2 (R) in Figure 3, the R_{IO} becomes broadband toward longer λ as the temperature increases. During the subsequent cooling process, the Bragg peak $\lambda_c \approx 1.49$ μm reappears as the dielectric state is restored and the photonic structure reverts to being a narrow-band NIR reflector. Figure 5b shows in more detail the reflectivity curves corresponding to the starting temperature T_{start_IO}, maximum temperature T_{max_IO}, and end temperature T_{end_IO} in this experiment. In addition, the electromagnetic simulation results for the VO_2 IO PhC in the dielectric VO_2 (M) phase (corresponding to the low temperatures, T_{start_IO}, and T_{end_IO}) and the metallic VO_2 (R) phase (corresponding to high temperature, T_{max_IO}) are compared with the experimental reflectance spectra, showing a good agreement, particularly in the general position and relative intensity of the Bragg peaks. Minor deviations between simulation and experiment mainly stem from the fact that the macropore size has a certain distribution, the existence of cracks, and the roughening of the surface of the VO_2 shell due to the annealing, resulting in diffuse scattering beyond the microscope's aperture. The Bragg peak's position λ_c during the temperature-dependent measurement from Figure 5a is presented in processed form in Figure 5c, revealing a reversible switch with external temperature. Specifically, when VO_2 is in the VO_2 (M) phase (low temperature), only the PBG near 1.49 μm in the IO exists. But it switches off at high temperatures when the VO_2 is in the VO_2 (R) phase. The situation of the PBG near 1.03 μm is just the opposite. Similarly, there is a hysteresis in this switching, which is consistent with the other fixed positions of R_{IO} in Figure S13. Besides, the variation of R_{IO} with temperature also exhibits a hysteresis, which is wider than that observed in thin films (Figure S13). Earlier reports show that the hysteresis of VO_2 in thin films can be altered by introducing either tensile or compressive strain, resulting in a narrower or wider hysteresis, respectively.[58,59] The 20% shrinkage observed during synthesis likely introduced residual stresses, which may differ from those of the thin film due to the different underlying substrates. While the thin film is prepared on top of a silicon substrate, the IO is assembled on top of a glass microscope glass substrate. Moreover, they have different thicknesses of around 0.5 mm for the Si wafer against 1 mm of the glass, likely leading to a lower surface temperature of the IO during measurement in comparison to the thin film since the heating plate heats them from underneath the substrate. All combined results in a wider IMT hysteresis in the VO_2 IO.

CONCLUSIONS

We successfully prepared high-quality polycrystalline VO_2 thin films via ALD combined with a postdeposition annealing treatment. Furthermore, the synthesis route was then adapted to conformally coat opaline PS templates, resulting in the successful fabrication of switchable VO_2 IO PhCs. The VO_2 thin films demonstrated an IMT in structural, electrical, and optical properties at about 60−70 °C, similar to previously reported VO_2 thin films obtained by other methods, e.g., magnetron sputtering, molecular beam epitaxy, and sol−gel. The integration of the VO_2's IMT properties with the IO PhCs structure opens active capabilities other than conventional photonics. Our VO_2 IO PhC exhibits a reversible switching between two different bandgaps at nearly 1.49 and 1.03 μm at low-temperature dielectric state and high-temperature metallic state, respectively. This work provides a convincing example of the integration of ALD-based VO_2 coating and devices with complex structures, holding significant promise for further unleashing the potential of VO_2 as the route herein described can be applied to other low-temperature substrates such as 3D-printed polymers.

MATERIALS AND METHODS

Thin Film Fabrication. The VO_2 thin film fabrication process involves two steps. Initially, a nonstoichiometric VO_x layer was deposited via thermal ALD in exposure mode, utilizing a modified Savannah100 reactor (Cambridge Nanotech). The deposition was conducted at 95 °C with 30 sccm (standard cubic centimeter per minute) nitrogen as carrier gas and purge gas. The working pressure during deposition was approximately 1.5 Torr. Various substrates including SiO_2/Si wafers and pure polished Si wafers (SIEGERT WAFER GmbH) were employed for coating. The precursors, deionized water and tetrakis(dimethylamino)vanadium(IV) (TDMAV, Strem Chemicals, Inc., USA) were utilized as oxygen and vanadium sources, respectively. The combination of "precursor pulse time/exposure time/purge time" was set as 0.1/15.0/60.0 s for deionized water and 1.0/15.0/60.0 s for TDMAV. Subsequently, the VO_x film was annealed at 425 °C in a vacuum oven (MC050, ANNEALsys) at 0.1 Torr for 10 min within a controlled atmosphere (10 sccm O_2, 100 sccm N_2).

VO_2 IO PhC Fabrication. The vertical self-assembly of the 757 nm diameter polystyrene beads (Microparticles GmbH) into an opal structure with FCC stacking followed a previously published procedure.[57] Next, the template was placed in the ALD chamber

https://doi.org/10.1021/acsami.4c13789
ACS Appl. Mater. Interfaces 2024, 16, 67106−67115

and coated by VO_x at 95 °C with a prolonged exposure time and purge time, i.e., 0.1/60.0/90.0 and 1.0/60.0/90.0 s, for deionized water and TDMAV, respectively. These parameters were set to enhance precursor penetration into the voids within the template, based on our previous studies on titania and mullite.[48,60] Following this, a portion of the top layer of the coated sample was etched by using a reactive ion etching system (SENTECH SI 500) via Ar ion sputtering. Afterward, template removal, coupled with a postdeposition annealing process, was conducted in the vacuum oven (MC050, ANNEALsys) to achieve the VO_2 phase in the 3D structure of the IO PhC. The annealing cycle consisted of two steps: (1) Controlled PS template removal to avoid potential phase changes from the VO_x phase to the V_2O_5 phase or distortion of the 3D structure in the second step. Specifically, the template removal was performed at 390 °C, near the polystyrene vaporization point, with a 1 °C/min heating rate in a vacuum of 0.01 Torr and maintained for 6 h. (2) Then the temperature was tuned to 425 °C, 200 sccm N_2, and 10 sccm O_2 were input, and the pressure was maintained at 0.1 Torr for 20 min for the subsequent postdeposition annealing process to achieve VO_2 phase.

Thin Film Characterization. Water-diluted HCl (20:1) was used to etch the as-deposited film to prepare a step-edge for thickness measurements by a profilometer (DektakXT, Bruker). Atomic force microscopy (AFM, Dimension ICON, Bruker) was applied to determine the thin film's roughness. Electrical characterization was carried out in a Physical Property Measurement System (VersaLab, Quantum Design). The crystalline phases of the thin films were determined by grazing incidence X-ray diffraction analysis (Bruker AXS D8 Advance, Bruker) using Cu Kα radiation. The incident angle was 0.5°, with the range, step size, and step time set to 26.5 to 29.0°, 0.01°, and 2 s for the *in situ* measurements and 10° to 60°, 0.01°, and 2 s for the *ex situ* measurements. The *in situ* measurements were performed by using a high-precision hot stage (DHS 900, Anton Paar) and a heating controller (TCU 150, Anton Paar). Heating and cooling cycles were performed from 25 °C until 90 °C with increments of 5 °C per measurement. Before data collection, samples were allowed to equalize the temperature for 5 min at each temperature data point. To ensure that no other phase change occurred due to the heating/cooling cycles, the samples were analyzed *ex situ* at room temperature (25 °C) before and after the *in situ* measurements. Raman measurements were performed using Renishaw inVia Raman Microscope equipped with a 20× objective, 1200 grooves/mm grating, and an excitation wavelength of 532 nm at a laser power of 1.7 mW. The Raman system incorporated a homemade temperature controller comprising a thermoelectric power generator Peltier module (SP1848−27145, VGEBY), a copper water cooling unit, and a voltage source. The optical measurements of the thin films were performed with a spectroscopic ellipsometer (SE-2000, SEMILAB) equipped with a heating chamber (Linkam). All measurements were performed at an incidence angle of 65° within the wavelength range of 650 to 2150 nm. The sample consisted of a 138.6 nm VO_2 layer on a 2 nm native SiO_2 layer on a Si substrate. The sample was heated in an open chamber in an air atmosphere to mitigate the influence of windows during data collection, reaching temperatures of up to 88 °C in increments of approximately 2 °C with a 120 s holding time before starting the spectroscopy ellipsometry measurement. Temperature readings were calibrated by using a thermoelement (NiCr-Ni) attached to the upper surface of the sample. The $\tilde{\varepsilon}(\lambda)$ of the VO_2 layer was obtained from the measured ellipsometry angles (Psi and Delta) by mathematical inversion method[61] and afterward checked for consistency with Kramers−Kronig relations. Both methods are implemented by Semilab in their Spectroscopic Ellipsometry Analyzer (SEA) software.

Characterizations of VO_2 IO PhC. SEM images were taken via scanning electron microscopy (SEM, Supra 55 VP, Zeiss). FIB-preparation and transfer of the TEM-lamella to the *in situ* MEMS chip were done with a Thermo Fisher Helios G3 UC according to the standard lift-out procedure. Contacting of the lamella to the MEMS chip was performed with beam-induced platinum deposition. The *in situ* experiments were performed in a Thermo Fisher Talos F200X transmission electron microscope equipped with a Thermo Fisher NanoEx-i/v *in situ* TEM sample holder. TEM micrographs were recorded in BF-TEM mode at 200 kV and 10 nA beam current. SAED patterns were recorded at a camera length of 840 mm. Intensity profiles were extracted using Velox TEM software (Thermo Fisher). Control of Temperature and heat rate was done with NanoEx-control software. The reflection spectra of the IO PhC samples were recorded using an FT-IR spectrometer Vertex 70 combined with a microscope Hyperion 2000 (Bruker Optics) and a Linkam Heating chamber TS1500. During heating, increments of 5 °C were applied for each measurement within the temperature ranges of 20 to 60 °C and 90 to 105 °C. Additionally, a smaller increment of 2 °C was applied near the IMT temperature, specifically within the range of 60 to 86 °C. In the cooling stage, increments of 5 °C were set within the temperature ranges of 105 to 85 °C and 84 to 20 °C. Furthermore, a smaller increment of 2 °C was applied within the temperature range of 60 to 38 °C.

Electromagnetic Simulation. The simulations were performed using a Frequency Domain Solver with hexagonal unit cell boundary conditions from the CST Studio Suite (Dassault Systèmes). The simulation model (see Figure S14) is designed as follows: there are six consecutive layers of spheres of 566 nm diameter, which are assembled into an FCC lattice with the (111)-plane parallel to the surface. For VO_2, we applied the permittivity function obtained from the ellipsometry measurements of the thin film. Below the spheres, a glass substrate with ε = 2.25 was considered. The background is air.

■ ASSOCIATED CONTENT

Data Availability Statement

The data supporting the findings of this work are available within the article and its Supporting Information files. All other relevant data supporting the findings of this study are available from the corresponding author on request.

Supporting Information

The Supporting Information is available free of charge at https://pubs.acs.org/doi/10.1021/acsami.4c13789.

Additional experimental details, methods, and simulation details, including data figures, experimental setup, and explanation (PDF)

■ AUTHOR INFORMATION

Corresponding Author

Robert Zierold − *Center for Hybrid Nanostructures, Universität Hamburg, 22607 Hamburg, Germany;* orcid.org/0000-0003-0292-0970; Email: rzierold@physnet.uni-hamburg.de

Authors

Jun Peng − *Center for Hybrid Nanostructures, Universität Hamburg, 22607 Hamburg, Germany;* orcid.org/0009-0008-6282-3762

Julia Brandt − *Institute of Optical and Electronic Materials, Hamburg University of Technology, 21073 Hamburg, Germany;* orcid.org/0009-0002-1698-6612

Maurice Pfeiffer − *Institute of Optical and Electronic Materials, Hamburg University of Technology, 21073 Hamburg, Germany;* orcid.org/0009-0002-3767-6672

Laura G. Maragno − *Integrated Ceramic-Based Materials Systems Group, Hamburg University of Technology, 21073 Hamburg, Germany*

Tobias Krekeler − *Betriebseinheit Elektronenmikroskopie, Hamburg University of Technology, 21073 Hamburg, Germany*

Nithin T. James − *Integrated Ceramic-Based Materials Systems Group, Hamburg University of Technology, 21073 Hamburg, Germany;* orcid.org/0009-0001-3292-0405

https://doi.org/10.1021/acsami.4c13789
ACS Appl. Mater. Interfaces 2024, 16, 67106−67115

Julius Henf − *Institute of Optical and Electronic Materials, Hamburg University of Technology, 21073 Hamburg, Germany*
Christian Heyn − *Center for Hybrid Nanostructures, Universität Hamburg, 22607 Hamburg, Germany;* orcid.org/0000-0002-7147-4006
Martin Ritter − *Betriebseinheit Elektronenmikroskopie, Hamburg University of Technology, 21073 Hamburg, Germany*
Manfred Eich − *Institute of Optical and Electronic Materials, Hamburg University of Technology, 21073 Hamburg, Germany; Institute of Functional Materials for Sustainability, Helmholtz-Zentrum Hereon, 21502 Geesthacht, Germany*
Alexander Yu. Petrov − *Institute of Optical and Electronic Materials, Hamburg University of Technology, 21073 Hamburg, Germany; Institute of Functional Materials for Sustainability, Helmholtz-Zentrum Hereon, 21502 Geesthacht, Germany*
Kaline P. Furlan − *Integrated Ceramic-Based Materials Systems Group, Hamburg University of Technology, 21073 Hamburg, Germany;* orcid.org/0000-0003-4032-2795
Robert H. Blick − *Center for Hybrid Nanostructures, Universität Hamburg, 22607 Hamburg, Germany; Deutsches Elektronen-Synchrotron (DESY), 22607 Hamburg, Germany*

Complete contact information is available at: https://pubs.acs.org/10.1021/acsami.4c13789

Author Contributions

J.P. and R.Z. designed experiments; J.P. performed ALD growth and analyses; L.M., N.J. and K.F. performed the template self-assembly experiments design and execution, XRD measurement and analyses; M.P. performed the ellipsometry measurements and analysis; J.B and J.H performed the FTIR measurement and the simulations; T.K. performed the TEM characterization and analysis. All authors analyzed the data, as well as wrote and improved the manuscript. All have approved the final version of the manuscript.

Notes

The authors declare no competing financial interest.

■ ACKNOWLEDGMENTS

This work was funded by the Deutsche Forschungsgemeinschaft (DFG, German Research Foundation) − Projektnummer 192346071 − SFB 986 "Tailor-Made Multi-Scale Materials Systems". We thank Dassault Systèmes for providing us with their electromagnetic simulation software CST Studio Suite. Furthermore, we acknowledge support via EU COST Action NETPORE (CA20126). Furthermore, we acknowledge financial support from the Open Access Publication Fund of Universität Hamburg. Open Access funding enabled and organized by Projekt DEAL.

■ REFERENCES

(1) Joannopoulos, J. D.; Villeneuve, P. R.; Fan, S. H. Photonic crystals: Putting a new twist on light. *Nature* **1997**, *386* (6621), 143−149.
(2) Joannopoulos, J. D.; Johnson, S. G.; Winn, J. N.; Meade, R. D. *Photonic Crystals: Molding the Flow of Light*; Princeton University Press, 2008.
(3) Lee, G.-H.; Moon, H.; Kim, H.; Lee, G. H.; Kwon, W.; Yoo, S.; Myung, D.; Yun, S. H.; Bao, Z.; Hahn, S. K. Multifunctional materials for implantable and wearable photonic healthcare devices. *Nature Reviews Materials* **2020**, *5* (2), 149−165.
(4) Li, G.; Zhang, S.; Zentgraf, T. Nonlinear photonic metasurfaces. *Nature Reviews Materials* **2017**, *2* (5), No. 17010.
(5) Bogaerts, W.; Pérez, D.; Capmany, J.; Miller, D. A. B.; Poon, J.; Englund, D.; Morichetti, F.; Melloni, A. Programmable photonic circuits. *Nature* **2020**, *586* (7828), 207−216.
(6) Ko, J. H.; Yoo, Y. J.; Lee, Y.; Jeong, H.-H.; Song, Y. M. A review of tunable photonics: Optically active materials and applications from visible to terahertz. *iScience* **2022**, *25* (8), No. 104727.
(7) Zheng, C.; Simpson, R. E.; Tang, K.; Ke, Y.; Nemati, A.; Zhang, Q.; Hu, G.; Lee, C.; Teng, J.; Yang, J. K. W.; et al. Enabling active nanotechnologies by phase transition: from electronics, photonics to thermotics. *Chem. Rev.* **2022**, *122* (19), 15450−15500.
(8) Wuttig, M.; Bhaskaran, H.; Taubner, T. Phase-change materials for non-volatile photonic applications. *Nat. Photonics* **2017**, *11* (8), 465−476.
(9) Neubrech, F.; Duan, X.; Liu, N. Dynamic plasmonic color generation enabled by functional materials. *Science Advances* **2020**, *6* (36), No. eabc2709.
(10) Morin, F. J. Oxides which show a metal-to-insulator transition at the Neel temperature. *Phys. Rev. Lett.* **1959**, *3* (1), 34−36.
(11) Adler, D.; Feinleib, J.; Brooks, H.; Paul, W. Semiconductor-to-metal transitions in transition-metal compounds. *Phys. Rev.* **1967**, *155* (3), 851−860.
(12) Zylbersztejn, A.; Mott, N. F. Metal-insulator transition in vanadium dioxide. *Phys. Rev. B* **1975**, *11* (11), 4383−4395.
(13) Qazilbash, M. M.; Brehm, M.; Chae, B.-G.; Ho, P.-C.; Andreev, G. O.; Kim, B.-J.; Yun, S. J.; Balatsky, A. V.; Maple, M. B.; Keilmann, F.; et al. Mott transition in VO_2 revealed by infrared spectroscopy and nano-imaging. *Science* **2007**, *318* (5857), 1750−1753.
(14) Aetukuri, N. B.; Gray, A. X.; Drouard, M.; Cossale, M.; Gao, L.; Reid, A. H.; Kukreja, R.; Ohldag, H.; Jenkins, C. A.; Arenholz, E.; et al. Control of the metal−insulator transition in vanadium dioxide by modifying orbital occupancy. *Nat. Phys.* **2013**, *9* (10), 661−666.
(15) Chen, S.; Wang, Z.; Ren, H.; Chen, Y.; Yan, W.; Wang, C.; Li, B.; Jiang, J.; Zou, C. Gate-controlled VO_2 phase transition for high-performance smart windows. *Science Advances* **2019**, *5* (3), No. eaav6815.
(16) Sood, A.; Shen, X.; Shi, Y.; Kumar, S.; Park, S. J.; Zajac, M.; Sun, Y.; Chen, L.-Q.; Ramanathan, S.; Wang, X.; et al. Universal phase dynamics in VO_2 switches revealed by ultrafast operando diffraction. *Science* **2021**, *373* (6552), 352.
(17) Hu, P.; Hu, P.; Vu, T. D.; Li, M.; Wang, S.; Ke, Y.; Zeng, X.; Mai, L.; Long, Y. Vanadium oxide: phase diagrams, structures, synthesis, and applications. *Chem. Rev.* **2023**, *123* (8), 4353−4415.
(18) Wen, C.; Feng, L.; Li, Z.; Bai, J.; Wang, S.; Gao, X.; Wang, J.; Yao, W. A review of the preparation, properties and applications of VO2 thin films with the reversible phase transition. *Front. Mater.* **2024**, *11*, DOI: 10.3389/fmats.2024.1341518.
(19) Armstrong, E.; O'Sullivan, M.; O'Connell, J.; Holmes, J. D.; O'Dwyer, C. 3D vanadium oxide inverse opal growth by electrodeposition. *J. Electrochem. Soc.* **2015**, *162* (14), D605.
(20) Cueff, S.; John, J.; Zhang, Z.; Parra, J.; Sun, J.; Orobtchouk, R.; Ramanathan, S.; Sanchis, P. VO_2 nanophotonics. *APL Photonics* **2020**, *5* (11), No. 110901.
(21) Ke, Y.; Balin, I.; Wang, N.; Lu, Q.; Tok, A. I. Y.; White, T. J.; Magdassi, S.; Abdulhalim, I.; Long, Y. Two-dimensional SiO_2/VO_2 photonic crystals with statically visible and dynamically infrared modulated for smart window deployment. *ACS Appl. Mater. Interfaces* **2016**, *8* (48), 33112−33120.
(22) Muskens, O. L.; Bergamini, L.; Wang, Y.; Gaskell, J. M.; Zabala, N.; de Groot, C. H.; Sheel, D. W.; Aizpurua, J. Antenna-assisted picosecond control of nanoscale phase transition in vanadium dioxide. *Light: Science & Applications* **2016**, *5* (10), e16173−e16173.
(23) King, J.; Wan, C.; Park, T. J.; Deshpande, S.; Zhang, Z.; Ramanathan, S.; Kats, M. A. Electrically tunable VO_2−metal metasurface for mid-infrared switching, limiting and nonlinear isolation. *Nat. Photonics* **2024**, *18* (1), 74−80.
(24) Golubev, V. G.; Kurdyukov, D. A.; Pevtsov, A. B.; Sel'kin, A. V.; Shadrin, E. B.; Il'inskii, A. V.; Boeyink, R. Hysteresis of the photonic

band gap in VO_2 photonic crystal in the semiconductor-metal phase transition. *Semiconductors* **2002**, *36* (9), 1043−1047.

(25) Ibisate, M.; Golmayo, D.; López, C. Vanadium dioxide thermochromic opals grown by chemical vapour deposition. *Journal of Optics A: Pure and Applied Optics* **2008**, *10* (12), No. 125202.

(26) Pemble, M.; Povey, I.; Chalvet, F. Developments in the understanding of ALD processes and applications of ALD in critical technologies. *ECS Trans.* **2007**, *11* (7), 155.

(27) Rampelberg, G.; Deduytsche, D.; De Schutter, B.; Premkumar, P. A.; Toeller, M.; Schaekers, M.; Martens, K.; Radu, I.; Detavernier, C. Crystallization and semiconductor-metal switching behavior of thin VO_2 layers grown by atomic layer deposition. *Thin Solid Films* **2014**, *550*, 59−64.

(28) Peter, A. P.; Martens, K.; Rampelberg, G.; Toeller, M.; Ablett, J. M.; Meersschaut, J.; Cuypers, D.; Franquet, A.; Detavernier, C.; Rueff, J.-P.; et al. Metal-insulator transition in ALD VO_2 ultrathin films and nanoparticles: morphological control. *Adv. Funct. Mater.* **2015**, *25* (5), 679−686.

(29) Mattelaer, F.; Geryl, K.; Rampelberg, G.; Dobbelaere, T.; Dendooven, J.; Detavernier, C. Atomic layer deposition of vanadium oxides for thin-film lithium-ion battery applications. *RSC Adv.* **2016**, *6* (115), 114658−114665.

(30) Blanquart, T.; Niinistö, J.; Gavagnin, M.; Longo, V.; Heikkilä, M.; Puukilainen, E.; Pallem, V. R.; Dussarrat, C.; Ritala, M.; Leskelä, M. Atomic layer deposition and characterization of vanadium oxide thin films. *RSC Adv.* **2013**, *3* (4), 1179−1185.

(31) Bai, G.; Niang, K. M.; Robertson, J. Preparation of atomic layer deposited vanadium dioxide thin films using tetrakis-(ethylmethylamino) vanadium as precursor. *Journal of Vacuum Science & Technology A* **2020**, *38* (5), No. 052402.

(32) Wang, X.; Guo, Z.; Gao, Y.; Wang, J. Atomic layer deposition of vanadium oxide thin films from tetrakis(dimethylamino)vanadium precursor. *J. Mater. Res.* **2017**, *32* (1), 37−44.

(33) Lv, X.; Cao, Y.; Yan, L.; Li, Y.; Song, L. Atomic layer deposition of VO2 films with Tetrakis-dimethyl-amino vanadium (IV) as vanadium precursor. *Appl. Surf. Sci.* **2017**, *396*, 214−220.

(34) Prasadam, V. P.; Bahlawane, N.; Mattelaer, F.; Rampelberg, G.; Detavernier, C.; Fang, L.; Jiang, Y.; Martens, K.; Parkin, I. P.; Papakonstantinou, I. Atomic layer deposition of vanadium oxides: process and application review. *Materials Today Chemistry* **2019**, *12*, 396−423.

(35) Lee, W.-J.; Chang, Y.-H. Growth without postannealing of monoclinic VO_2 thin film by atomic layer deposition using VCl_4 as precursor. *Coatings* **2018**, *8* (12), 431.

(36) Gao, Y.; Shao, Y.; Yan, L.; Li, H.; Su, Y.; Meng, H.; Wang, X. Efficient charge injection in organic field-effect transistors enabled by low-temperature atomic layer deposition of ultrathin VO_x interlayer. *Adv. Funct. Mater.* **2016**, *26* (25), 4456−4463.

(37) Hausmann, D. M.; Kim, E.; Becker, J.; Gordon, R. G. Atomic layer deposition of hafnium and zirconium oxides using metal amide precursors. *Chem. Mater.* **2002**, *14* (10), 4350−4358.

(38) Li, J.; Guo, J.; Zhou, Z.; Xu, R.; Xu, L.; Ding, Y.; Xiao, H.; Li, X.; Li, A.; Fang, G. Atomic layer deposition mechanism of hafnium dioxide using hafnium precursor with amino ligands and water. *Surfaces and Interfaces* **2024**, *44*, No. 103766.

(39) Blankenship, B. W.; Li, R.; Guo, R.; Zhao, N.; Shin, J.; Yang, R.; Ko, S. H.; Wu, J.; Rho, Y.; Grigoropoulos, C. Photothermally activated artificial neuromorphic synapses. *Nano Lett.* **2023**, *23* (19), 9020−9025.

(40) Feng, C.; Li, B.-W.; Dong, Y.; Chen, X.-D.; Zheng, Y.; Wang, Z.-H.; Lin, H.-B.; Jiang, W.; Zhang, S.-C.; Zou, C.-W.; et al. Quantum imaging of the reconfigurable VO_2 synaptic electronics for neuromorphic computing. *Science Advances* **2023**, *9* (40), No. eadg9376.

(41) Evlyukhin, E.; Howard, S. A.; Paik, H.; Paez, G. J.; Gosztola, D. J.; Singh, C. N.; Schlom, D. G.; Lee, W.-C.; Piper, L. F. J. Directly measuring the structural transition pathways of strain-engineered VO_2 thin films. *Nanoscale* **2020**, *12* (36), 18857−18863.

(42) Moatti, A.; Sachan, R.; Cooper, V. R.; Narayan, J. Electrical Transition in Isostructural VO_2 Thin-Film Heterostructures. *Sci. Rep.* **2019**, *9* (1), 3009.

(43) Baum, P.; Yang, D.-S.; Zewail, A. H. 4D visualization of transitional structures in phase transformations by electron diffraction. *Science* **2007**, *318* (5851), 788.

(44) Petrov, G. I.; Yakovlev, V. V.; Squier, J. Raman microscopy analysis of phase transformation mechanisms in vanadium dioxide. *Appl. Phys. Lett.* **2002**, *81* (6), 1023−1025.

(45) Shvets, P.; Dikaya, O.; Maksimova, K.; Goikhman, A. A review of Raman spectroscopy of vanadium oxides. *J. Raman Spectrosc.* **2019**, *50* (8), 1226−1244.

(46) Angel, R. J.; Murri, M.; Mihailova, B.; Alvaro, M. *Stress, strain and Raman shifts* **2019**, *234* (2), 129−140.

(47) Parker, J. C. Raman scattering from VO_2 single crystals: A study of the effects of surface oxidation. *Phys. Rev. B* **1990**, *42* (5), 3164−3166.

(48) Kubrin, R.; Pasquarelli, R. M.; Waleczek, M.; Lee, H. S.; Zierold, R.; do Rosário, J. J.; Dyachenko, P. N.; Montero Moreno, J. M.; Petrov, A. Y.; Janssen, R.; et al. Bottom-up fabrication of multilayer stacks of 3D photonic crystals from titanium dioxide. *ACS Appl. Mater. Interfaces* **2016**, *8* (16), 10466−10476.

(49) Wei, J.; Ji, H.; Guo, W.; Nevidomskyy, A. H.; Natelson, D. Hydrogen stabilization of metallic vanadium dioxide in single-crystal nanobeams. *Nat. Nanotechnol.* **2012**, *7* (6), 357−362.

(50) Guo, Y.; Zhang, Y.; Zhang, L.; Lv, X.; Wu, L.; Cao, Y.; Song, L. Study of the phase transition properties and electronic band structures of VO_2 thin films grown on different substrates. *Materials Research Express* **2019**, *6* (2), No. 026409.

(51) Oguntoye, I. O.; Padmanabha, S.; Hinkle, M.; Koutsougeras, T.; Ollanik, A. J.; Escarra, M. D. Continuously tunable optical modulation using vanadium dioxide Huygens metasurfaces. *ACS Appl. Mater. Interfaces* **2023**, *15* (34), 41141−41150.

(52) Wan, C.; Zhang, Z.; Woolf, D.; Hessel, C. M.; Rensberg, J.; Hensley, J. M.; Xiao, Y.; Shahsafi, A.; Salman, J.; Richter, S.; et al. On the optical properties of thin-film vanadium dioxide from the visible to the far infrared. *Annalen der Physik* **2019**, *531* (10), No. 1900188.

(53) Mackay, T. G.; Lakhtakia, A. *The Transfer-Matrix Method in Electromagnetics and Optics*; Springer: Cham, 2020.

(54) Maier, S. A. *Plasmonics: Fundamentals and Applications*; Springer: 2007.

(55) Gehensel, R. J.; Zierold, R.; Schaan, G.; Shang, G.; Petrov, A. Y.; Eich, M.; Blick, R.; Krekeler, T.; Janssen, R.; Furlan, K. P. Improved thermal stability of zirconia macroporous structures via homogeneous aluminum oxide doping and nanostructuring using atomic layer deposition. *Journal of the European Ceramic Society* **2021**, *41* (7), 4302−4312.

(56) Pasquarelli, R. M.; Lee, H. S.; Kubrin, R.; Zierold, R.; Petrov, A. Y.; Nielsch, K.; Schneider, G. A.; Eich, M.; Janssen, R. Enhanced structural and phase stability of titania inverse opals. *Journal of the European Ceramic Society* **2015**, *35* (11), 3103−3109.

(57) Furlan, K. P.; Larsson, E.; Diaz, A.; Holler, M.; Krekeler, T.; Ritter, M.; Petrov, A. Y.; Eich, M.; Blick, R.; Schneider, G. A.; et al. Photonic materials for high-temperature applications: Synthesis and characterization by X-ray ptychographic tomography. *Applied Materials Today* **2018**, *13*, 359−369.

(58) Jeong, J.; Aetukuri, N.; Graf, T.; Schladt, T. D.; Samant, M. G.; Parkin, S. S. P. Suppression of metal-insulator transition in VO_2 by electric field-induced oxygen vacancy formation. *Science* **2013**, *339* (6126), 1402−1405.

(59) Chen, H.-W.; Li, C.-I.; Ma, C.-H.; Chu, Y.-H.; Liu, H.-L. Strain engineering of optical properties in transparent VO_2/muscovite heterostructures. *Phys. Chem. Chem. Phys.* **2021**, *23* (14), 8908−8915.

(60) Furlan, K. P.; Krekeler, T.; Ritter, M.; Blick, R.; Schneider, G. A.; Nielsch, K.; Zierold, R.; Janßen, R. Low-temperature mullite formation in ternary oxide coatings deposited by ALD for high-temperature applications. *Advanced Materials Interfaces* **2017**, *4* (23), No. 1700912.

(61) Fujiwara, H. *Spectroscopic Ellipsometry: Principles and Applications*; Wiley, 2007.

https://doi.org/10.1021/acsami.4c13789
ACS Appl. Mater. Interfaces 2024, 16, 67106−67115